



## Electrochemically reconstructed perovskite with cooperative catalytic sites for CO<sub>2</sub>-to-formate conversion

Meng-Nan Zhu<sup>a</sup>, Bo-Wen Zhang<sup>a</sup>, Min-Rui Gao<sup>a</sup>, Peng-Fei Sui<sup>a</sup>, Chenyu Xu<sup>a</sup>, Lu Gong<sup>a</sup>, Hongbo Zeng<sup>a</sup>, Karthik Shankar<sup>b</sup>, Steven Bergens<sup>c</sup>, Jing-Li Luo<sup>a,\*</sup>

<sup>a</sup> Department of Chemical and Materials Engineering, University of Alberta, Edmonton, Alberta T6G 1H9, Canada

<sup>b</sup> Department of Electrical and Computer Engineering, University of Alberta, Edmonton, Alberta T6G 1H9, Canada

<sup>c</sup> Department of Chemistry, University of Alberta, Edmonton, Alberta T6G 1H9, Canada



### ARTICLE INFO

#### Keywords:

Carbon dioxide reduction reaction (CO<sub>2</sub>RR)  
Perovskites  
Electrocatalysts reconstruction  
Alkaline metal cations  
Photoelectrocatalysis

### ABSTRACT

Perovskites are the promising catalysts for various reactions, yet their structure evolutions and the composition-function relation in the carbon dioxide reduction reaction (CO<sub>2</sub>RR) are not fully explored. In this study, we report that the reconstructed BaBiO<sub>3</sub> (BBO) perovskite is able to facilitate CO<sub>2</sub>-to-formate (FA) conversion by both A-(Ba) and B- (Bi) site elements through the cooperative but distinct catalytic mechanisms. Specifically, the electrochemical reductions of BBO trigger the complete rearrangement of atoms with rapid kinetics at catalytically relevant voltages, giving rise to electricity-induced Bi metallene (eBBO) that efficiently generates FA with high selectivity and partial current densities. Moreover, the reconstructed BBO simultaneously enables Ba<sup>2+</sup> release to the electrolyte, and the time-resolved FTIR and *in situ* Raman analysis collectively reveal that the Ba<sup>2+</sup> adsorption enables easier CO<sub>2</sub> adsorption, thereby leading to enhanced CO<sub>2</sub>-to-FA conversion. This work is of direct significance in elucidating the cooperative catalysis between A- and B- site elements in perovskites for room-temperature CO<sub>2</sub>RR.

### 1. Introduction

Carbon dioxide reduction reaction (CO<sub>2</sub>RR) driven by sustainable energy resources holds great promise for alleviating the adverse effects of CO<sub>2</sub> accumulation by converting CO<sub>2</sub> to value-added chemicals in order to realize zero net emission of CO<sub>2</sub> in the carbon cycle of CO<sub>2</sub>-fuel-CO<sub>2</sub> [1–4]. Formate/Formic acid (HCOO<sup>−</sup>, FA) is an important liquid product of CO<sub>2</sub>RR and plays an indispensable part in various industrial processes [5–8]. For the past few years, substantial efforts have been devoted to boosting the CO<sub>2</sub>-to-FA conversion using different nanostructured catalysts, however, the complicated synthesis procedures and low product yields are usually associated with many of these catalysts, which hinder their scalability. Therefore, it is imperative to synthesize electrocatalysts through rational design with easy fabrication process and economic feasibility to advance CO<sub>2</sub>RR technology for its large-scale implementation.

Inspired by the multiple advantages of perovskites (e.g., structural/compositional flexibility, good scalability, etc.), we pursue initiating the room-temperature electrochemical conversion of CO<sub>2</sub> on perovskite-

based catalysts owing to their excellent activity and easy production [9–11]. It has been well recognized that B-site cations of perovskites play major catalytic roles, and this knowledge provides a basis when choosing appropriate perovskite. For instance, Cu-based perovskites have been shown to favorably produce hydrocarbon products, i.e. CH<sub>4</sub> [12], C<sub>2</sub>H<sub>4</sub> [13], while Sn-based perovskites, in sharp contrast, tend to selectively produce FA [14]. According to these studies, a close correlation can be established between the type of B-site species and production distributions in CO<sub>2</sub>RR. The second concern needs to be addressed is the potential-induced reconstruction of perovskites at catalytically relevant voltages. Electricity-driven reconstructions in electrocatalysts have been actively investigated in binary metal compounds (i.e., oxides, sulfides, etc.) for various applications including oxygen evolution reaction (OER), hydrogen evolution reaction (HER), etc. [15–17], but rarely discussed in perovskites for room-temperature CO<sub>2</sub>RR. In general, the voltage-driven reconstructions in perovskites could lead to the change of crystal phase accompanied by the evolution of geometrical structures (i.e., enlarged surface area, more exposed active sites, etc.); and/or give rise to new electronic features that

\* Corresponding author.

E-mail address: [jingli.luo@ualberta.ca](mailto:jingli.luo@ualberta.ca) (J.-L. Luo).

stabilize certain intermediates and lead to the promoted activity of reactions [18–22]. Finally, it should be noted that the electrochemical reduction of perovskite will trigger the rearrangement of all or a portion of A-site elements due to the “diffusion - re-nucleation - growth” of B-site ions [23,24]. Since A-site elements in perovskites are usually considered to be non-active in CO<sub>2</sub>RR (i.e., Pr, Ba, La, and Sr, etc.), the role of A-site elements in CO<sub>2</sub> conversion under room-temperature conditions has been overlooked so far. Therefore, the reconstructions of perovskites under cathodic potentials may be of great significance for CO<sub>2</sub>RR and require further investigations.

In this work, a BaBiO<sub>3</sub> (BBO) perovskite is fabricated by crystallization of the sol-gel Ba<sup>2+</sup>/Bi<sup>3+</sup> nitrate crosslinkers. Bi cations placed at B-site is expected to facilitate FA production, whereas Ba at A-site is determined due to its suitable ionic radius and valence state to form perovskite structure. Our studies show that under negative potentials, BBO pre-catalysts undergo irreversible structural and phase transformations, giving rise to electricity-induced Bi metallene (eBBO) that leads to high FA selectivity in both electrochemical (EC) and photo-electrochemical (PEC) cells. Further investigations reveal that A-site element (Ba) can diffuse to the electrolyte and remain as Ba<sup>2+</sup> ions, and the effects of Ba<sup>2+</sup> on CO<sub>2</sub>RR are co-dependent on the type of electrolyte, the external potentials, and the concentration of Ba<sup>2+</sup> in the electrolyte. Our study proposes that the utilization of both A- and B-sites in BBO to benefit CO<sub>2</sub> conversion could be possible, which may be extended to other perovskite electrocatalysts for CO<sub>2</sub>RR.

## 2. Experimental section

### 2.1. Materials preparation

Commercial Bi nanoparticles (granular, ≥ 99.99%) were purchased from Sigma-Aldrich. BaBiO<sub>3</sub> (BBO) powder was prepared by a modified sol–gel method. Stoichiometric amounts of Ba(NO<sub>3</sub>)<sub>2</sub> and Bi (NO<sub>3</sub>)<sub>3</sub>·5H<sub>2</sub>O were firstly dissolved in 300 mL deionized water (DIW) and then, nitric acid was introduced dropwise until Bi(NO<sub>3</sub>)<sub>3</sub>·5H<sub>2</sub>O was completely dissolved. Afterwards, EDTA and citric acid were added (the molar ratio of EDTA and citric acid to total metal ions was set as 1:2:1), and the pH of the solution was adjusted to be around 7 by NH<sub>3</sub>·H<sub>2</sub>O. The precursor solution was slowly evaporated on a hot plate to yield viscous gel which further underwent a self-combustion reaction. Finally, the obtained powder was annealed at 850 °C for 4 h in air, and the as-obtained powder was further ball milled in ethanol for 6 h to achieve smaller particle size distribution.

Nanoporous BiVO<sub>4</sub> (BVO) photoanode was prepared according to the pioneering work by Kim and Choi with slight modifications [25]. Briefly, 0.73 g Bi(NO<sub>3</sub>)<sub>3</sub>·5H<sub>2</sub>O was dissolved in 50 mL 0.4 M KI solution, its pH was adjusted to ~ 1.7 by HNO<sub>3</sub>. The precursor was further mixed with a separate ethanol solution (20 mL) containing 0.23 M p-benzoquinone and stirred for 5 mins to form the BiOI deposition precursor solution. To obtain BiOI nanosheets, a piece of clean FTO (2 \* 3 cm<sup>2</sup>), Pt foil and Ag/AgCl (sat.) electrode were employed as the working, counter, and reference electrodes, respectively. The potential was kept at - 0.1 V vs. Ag/AgCl for 10–12 min to deposit BiOI. To convert BiOI to BiVO<sub>4</sub>, 0.6 mL of 0.2 M VO(acac)<sub>2</sub> dissolved in DMSO was pipetted onto BiOI, which was further annealed at 450 °C for 2 h at a ramping rate of 2 °C min<sup>-1</sup>. Afterwards, the as-obtained material was soaked in 1.0 M KOH for 30 mins to remove excess V<sub>2</sub>O<sub>5</sub>. Finally, the BVO substrate was dried and annealed at 270 °C at a ramping rate of 2 °C min<sup>-1</sup> in Ar/H<sub>2</sub>(5%) for 20 min to generate excessive oxygen vacancies (BVOh). FeOOH and NiOOH co-catalyst layer was further deposited on BVOh to enhance water oxidation kinetics. FeOOH thin layer was photo-deposited onto BiVO<sub>4</sub> from a 0.1 M FeSO<sub>4</sub> solution. To assist photo-deposition, an external bias of 0.3 V vs. Ag/AgCl was applied. The deposition proceeded for 20 mins prior to increasing the potential to 1.2 V vs. Ag/AgCl and maintained there for another 1 min. Subsequently, NiOOH was photo-deposited from a 0.1 M NiSO<sub>4</sub> solution (pH ~ 7) with an external

potential of 0.11 V vs. Ag/AgCl for 15 mins, followed by a sequential electrodeposition of NiOOH at 1.2 V vs. Ag/AgCl for 1 min. The as-prepared samples are denoted as BVOh-FN. The BVOh-FN photo-electrode was washed with deionized water (DIW), and naturally dried overnight.

### 2.2. Materials characterizations

The X-ray diffraction (XRD) spectra were acquired on a Rigaku Ultima IV equipped with a Cu-K $\alpha$  radiation source ( $K\alpha = 1.540598 \text{ \AA}$ ) operating at 40 kV and 44 mA (scan speed: 8 min<sup>-1</sup>). For the postmortem XRD analysis, 0.1 g BBO were mixed with 0.025 g carbon black (Cabot Corp. vxc72) and dispersed in IPA and then dip-casted on glassy-carbon electrode to reach a loading amount of 1.0 mg cm<sup>-2</sup> for electroreduction. The as-prepared catalysts were scrapped off from the electrode surface and dried in vacuum prior to characterizations. *In situ* and *ex situ* Raman analysis were conducted on Renishaw inVia Qontor Confocal Raman Microscope with a laser wavelength of 532 nm. Field emission scanning electron microscope (FESEM) was performed using Zeiss Sigma FESEM. Transmission electron microscope (TEM) analysis was conducted using JEOL JEM-ARM200CF equipped with the Energy-dispersive X-ray (EDX) detector. X-ray photoelectron spectroscopy (XPS) was carried out on Kratos AXIS to study the surface chemistry of materials. All the XPS spectra were referenced to the C 1s binding energy of 284.8 eV and fitted using Shirley baselines. Fourier-transform infrared spectroscopy (FTIR) was performed on the Nicolet 8700 Fourier Transform Infrared Spectrometer equipped with an in situ cell with constant CO<sub>2</sub>/H<sub>2</sub> flow (CO<sub>2</sub>: H<sub>2</sub> = 0.2: 20 sccm) during signal collections. Prior to measurements, the sample was blown with Helium at a flow rate of 20 sccm for 1 h until the signals reached a stable state. For samples preparation, pristine BBO powder was mixed with carbon black in a mass ratio of 5: 1 to prepare the catalyst ink. The ink was then coated on a piece of clean FTO to achieve a loading mass of 1.0 mg cm<sup>-2</sup>, and then electrochemically reduced at - 1.2 V for 3000 s to produce eBBO electrode. The sample was then washed thoroughly with DIW and dried over night before test. To prepare Ba<sup>2+</sup> loaded samples (Ba<sup>2+</sup>-eBBO), BaCl<sub>2</sub> was dissolved in DIW to prepare the 0.1 M stock solution and then dipped onto the electrode surface with the stoichiometric amounts of Ba: Bi = 1: 1.

### 2.3. CO<sub>2</sub> reduction analysis

To prepare the catalyst ink for CO<sub>2</sub>RR, 10 mg of BBO and 10 mg of carbon black were grounded in a mortar and then dispersed in 0.5 mL of solvent containing 0.45 mL ethanol and 0.05 mL Nafion solution (5 wt%, Sigma-Aldrich), followed by a consistent ultrasonic treatment for 2 h. Then, 0.05 mL of the as-prepared ink was pipetted onto carbon paper to yield a loading mass of 1.0 mg cm<sup>-2</sup>. The electrochemical CO<sub>2</sub>RR was performed in a three-electrode H-type cell with a piece of BBO, graphite rod and Ag/AgCl (sat.) electrode as the working, counter, and reference electrodes, respectively. The volume of the electrolyte in each compartment is 35 mL. All the potentials reported were converted to a reversible hydrogen electrode (RHE):  $E_{\text{RHE}}(\text{V}) = E_{\text{Ag/AgCl}}(\text{V}) + 0.059 \cdot \text{pH} + 0.197$ . Electrochemical studies were performed using an Autolab electrochemical workstation. Cyclic voltammetry analysis (CV) was conducted in Argon-saturated 0.1 M KHCO<sub>3</sub>, and double layer capacitance measurement studies were performed in non-Faradaic current region at various scan rates (10, 20, 40, 60, 80, 100, and 120 mV s<sup>-1</sup>). The double layer capacitance ( $C_{dl}$ ) values of catalysts were extrapolated from half of the slope of  $\Delta j/2$  versus. scan rate plot. The electrochemically active surface area (ECSA) was determined by the following equation:  $\text{ECSA} = R_f \times S$ , where  $R_f$  and  $S$  stand for the surface roughness and the real surface area of the electrode ( $S = 1 \text{ cm}^2$ ), respectively.  $R_f$  is defined as the ratio of the  $C_{dl}$  value of a catalyst electrode (denoted as  $C_{dl}$  - catalyst) to that of a reference electrode (denoted as  $C_{dl}$  - reference). In this case, a piece of blank carbon paper with a geometric surface area of

1 cm<sup>2</sup> coated with 0.05 mL of the ethanol and Nafion mixture solution (8:1 in volume ratio) was used as the reference electrode [26,27]. Clearly, the ECSA area of the catalyst electrode scales up linearly with the value of C<sub>dl</sub> - catalyst for the same C<sub>dl</sub> - reference and S. Linear sweep voltammetry (LSV) polarization curves were recorded in either Argon or CO<sub>2</sub> saturated electrolytes with a scan rate of 50 mV s<sup>-1</sup>. For PEC CO<sub>2</sub>RR, a collimated beam solar simulator with an air 503 mass 1.5 G filter was used as the light source to acquire the photo-responses under irradiation (SCIENCETECH). The electrochemical characterizations of BVO<sub>x</sub>-FN were performed in the same three-electrode cell with 0.1 M KHCO<sub>3</sub> electrolyte. For the full cell characterizations, a two-electrode cell was employed.

#### 2.4. Product quantification

##### 2.4.1. Gaseous products

the Agilent 6890 N gas chromatograph (GC) equipped with a thermal conductivity detector (TCD) and a flame ionization detector (FID) was employed to detect gaseous products. Faradaic efficiency for product x ( $FE_x$ , x = CO, and H<sub>2</sub>) was calculated based on Eq. 1:

$$FE_x = \frac{i_x}{i_{total}} = \frac{n_x \cdot \nu_{CO_2} \cdot c_x \cdot F \cdot V_m^{-1}}{i_{total}} \quad (1)$$

Where  $i_x$  and  $i_{total}$  stand for the partial current density of product x and the overall current flowed through the system;  $n_x$  represents the number of electron transfer for the formation of 1 mol of x;  $\nu_{CO_2}$  denotes the flow rate (sccm) of CO<sub>2</sub> feeding gas, which is 20 sccm in this study;  $c_x$  is the concentration (p.p.m) of x detected by GC; F and  $V_m^{-1}$  refer to the Faraday constant (96,485 C mol<sup>-1</sup>) and unit molar volume (24.5 L mol<sup>-1</sup>) at 298.15 K.

##### 2.4.2. Liquid product

the liquid product was quantified by Metrohm 850 Professional IC Cation-HP-Gradient (Ion Chromatography). Faradaic efficiency for HCOO<sup>-</sup> ( $FE_{HCOO^-}$ ) was calculated based on Eq. 2:

$$FE_{HCOO^-} = \frac{2 \cdot c_{HCOO^-} \cdot V \cdot e \cdot N_A \cdot (0.001)}{Q_{total}} \quad (2)$$

Where  $c_{HCOO^-}$  (mol L<sup>-1</sup>) is the measured concentration of HCOO<sup>-</sup>; V stands for the total volume of the electrolyte, which is 35 mL in this study; e is  $1.6 \times 10^{-19}$  C mol<sup>-1</sup>;  $N_A$  is the Avogadro Number ( $6.02 \times 10^{23}$ );  $Q_{total}$  represents the total amount of charge passed through the system.

#### 2.5. Computational methods

Density-Functional-Theory (DFT) calculations were performed using Vienna Ab initio Simulation Package. Vaspkit package was used to generate input files [28]. Perdew-Burke-Ernzerhof within the generalized gradient approximation was employed to describe the electronic interactions. For unit cell optimization, a cutoff energy of 520 eV was set. Spin polarization was considered in all calculations. Based on the optimized cells, the following calculations were performed on a (3 × 3) Bi (003) slab, (3 × 1) BBO (100) and (3 × 1) BBO (001) slab with a 15 Å vacuum layer on the top (Table S1). Brillouin Zone k points (3 × 3 × 1), (6 × 5 × 1) and (4 × 5 × 1) were generated for Bi (003) slab, BBO (100) and BBO (001) slab, respectively, and the cutoff energy was set as 500 eV. The criterion of convergence for electronic step was set as  $10^{-5}$ . The two upper layers of the slab were allowed to fully relax until a maximum force component of 0.02 eV/Å was reached, meanwhile, the positions of other atoms were fixed. To obtain the optimized model with \*OCHO adsorption, the different supercell models with various adsorption locations was considered, and the configuration with the lowest energy was used in the subsequent calculations (Table S2). The Gibbs free energy of the slabs with different adsorbents was

determined by:  $G = E_{DFT} + E_{ZPE} + \int C_p dT - TS$ , where  $E_{DFT}$ ,  $E_{ZPE}$ ,  $\int C_p dT$  and TS stand for the DFT calculated electronic energy, zero-point energy, enthalpy correction and entropy correction, respectively. Finally, to obtain the Gibbs free energy change in each step of the CO<sub>2</sub>RR and HER, the computational hydrogen electrode model (CHE) was employed (Supporting Information, Note 1) [29].

### 3. Results and discussion

#### 3.1. Structure characterizations of BaBiO<sub>3</sub>

Gram-scale BBO powder was synthesized by annealing 0.01 mol BBO sol-gel precursor under high temperature followed by ball-milling for 6 h to achieve the smaller particle size distributions of BBO (Fig. S1), and 0.01 mol of BBO precursor could roughly yield 2.9 g BBO raw powder. Crystalline BBO possesses the monoclinic ABO<sub>3</sub> perovskite structure where the Ba atoms sit in the tunnel enclosed by the distorted [BiO<sub>6</sub>] octahedra connected through the corner oxygen atoms. The X-ray diffraction (XRD) pattern of the sintered powder matches well with the standard monoclinic BBO phase (JCPDS: 035–1020, Fig. 1a) with no discernable second-phase. The successful synthesis of BBO is further corroborated by the Raman scattering spectrum where the three fingerprint vibrations emerged at 300.0, 492.1, and 556.4 cm<sup>-1</sup> can be well assigned to the superposition of Bi-O bending mode, Bi-O stretching mode, and the [BiO<sub>6</sub>] breathing with A<sub>g</sub> symmetry in monoclinic BBO, respectively (Fig. 1b) [30]. To probe the morphological and structural features of the ball-milled BBO, the field-emission scanning electron microscopy (FESEM) and transmission electron microscopy (TEM) were carried out. The results reveal that the ball-milled BBO composes of the irregularly-shaped nanoparticles (Fig. 1c, d, and S2), and the uniform distribution of Ba, Bi, and O across the whole BBO architecture has been confirmed by the energy dispersive X-ray (EDX) mappings of elements (Fig. S3). The physical characterizations indicate that sol-gel method is suitable for synthesizing homogeneous BBO powder with high yields from the single batch reaction.

#### 3.2. Electricity-induced reconstruction of BaBiO<sub>3</sub>

Considering the cathodic working potential nature of CO<sub>2</sub>RR, we performed the CV analysis to initially probe the redox capabilities of fresh BBO (Fig. 1e and S4). No distinguishable reduction peak could be observed in the initial cathodic sweep, but starting from the second scan, a cathodic peak merged at 0.04 V, indicative of the reduction of Bi ions. Notably, the inter-crossing point located at -0.07 V is attributed to the insulating nature of BBO and the high energy requirement to deconstruct BBO scaffold [31]. In anodic scans, three anodic peaks located at 0.23 V (point C), 0.43 V (point D) and 0.63 V (point E) represent the oxidation reactions from Bi<sup>0</sup> to Bi<sup>3+</sup>. The gradually overlapped CV curves demonstrate that the BBO pre-catalyst has reached an electrochemically steady state upon successive Bi<sup>0</sup>/Bi<sup>3+</sup> cycling. The presence of Bi<sup>0</sup> phase is further supported by performing the XRD analysis over cathodically reduced BBO electrodes at -1.2V for various time periods of 100, 500, 1000, 3000 and 5000 s (denoted as BBO100, BBO500, BBO1000, BBO3000, and BBO5000, respectively, Fig. 1f). The peaks emerged at 23.8°, 27.2°, 37.9° and 39.6° are well indexed to the (003), (012), (104) and Bi (110) facets of metallic Bi, respectively, thus confirming the formation of rhombohedral Bi<sup>0</sup> (JCPDS: 44–1426) in all reduced BBO samples. Notably, the readily observed Bi<sup>0</sup> phase in BBO100 imply that voltage-driven Bi reduction is an extremely efficient process compared to the traditional high-temperature annealing method in reducing atmosphere (which usually takes up to hours) [24]. Based on these results, we further performed Raman spectroscopy over a typical phase-changed BBO3000 (Fig. 1g). Clearly, the absence of all three representative BBO Raman shifts in BBO3000 confirms the deconstruction of BBO architecture upon deep reductions. The surface chemistry of BBO3000 was studied by the X-ray photoelectron spectroscopy (XPS). As

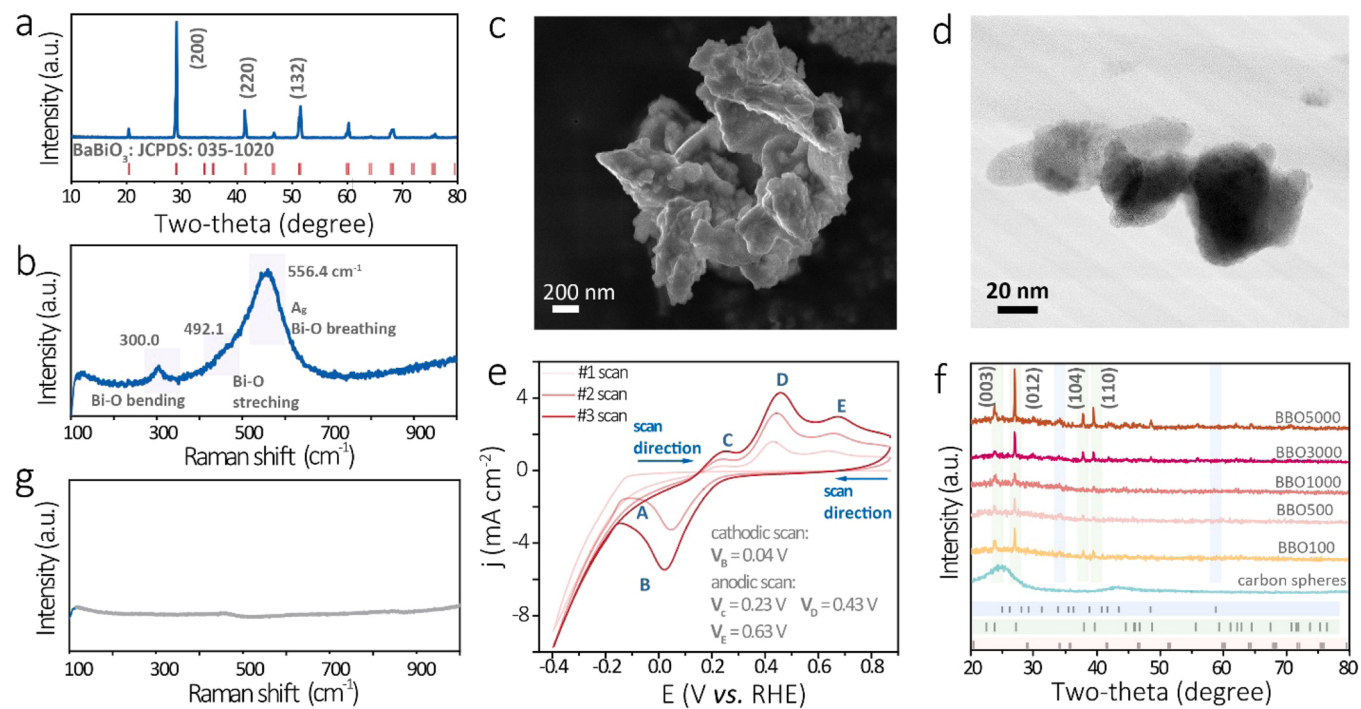


**Fig. 1.** (a) XRD pattern, (b) Raman spectrum, (c) FESEM, and (d) TEM images of fresh BBO powder. (e) CV curves of fresh BBO electrode. (f) *Ex situ* XRD analysis of BBO electrodes reduced at various time periods of 100, 500, 1000, 3000, and 5000 s (green: JCPDS Bi: 44–1246; blue: JCPDS  $\text{Bi}_2\text{O}_2\text{CO}_3$ : 41–1448; red: JCPDS  $\text{BaBiO}_3$ : 035–1020). (g) Raman spectrum of BBO3000.

shown in Fig. S5a and S5b, the Bi 4f spectra of BBO3000 and the control sample Bi-3000 (where the commercial Bi nanoparticles were reduced at -1.2 V for 3000 s) exhibit the similar features, and the two peaks located at around 159 eV and 164 eV can be ascribed to the  $\text{Bi}^{\delta+}$  ( $0 < \delta < 3$ ) resulting from the oxidation of surface Bi species [32,33]. The surface oxides of the BBO3000 and Bi-3000 were then partly removed by the  $\text{Ar}^+$  sputter etching for three minutes (denoted as BBO3000-etch and metal Bi-3000-etch, respectively). After surface etching, the original XPS peaks split into four new peaks. The new peaks located at around 157.1 and 162.4 eV can be ascribed to metallic Bi; the other two peaks at around 159.6 and 165.0 eV can be assigned to  $\text{Bi}^{3+}$ . The resembled Bi 4 f scans of eBBO and metal Bi suggest similar chemical states of Bi atoms in eBBO and metallic Bi. These results confirm that the fresh BBO was reduced to  $\text{Bi}^0$  phase when subjected to the external potential of -1.2 V for 3000 s. Moreover, the Ba signals are completely vanished after cathodic polarization, as observed from both XPS (Fig. S5c and S5d) and Raman analysis, which is presumably explained by the release of  $\text{Ba}^{2+}$  into the surrounding electrolyte, rather than the formation of relevant Ba species (i.e.,  $\text{BaO}$ ) at the electrode surface, which we will return to shortly.

*Ex situ* FESEM images of the different BBO samples during the reduction process were captured to examine the surface morphology changes (Fig. S6). Upon a short reduction time of 100 s, no apparent morphological changes have been observed, but the surface of BBO100 is clearly roughened, which is assigned to the partial Bi exsolution from BBO lattice. Starting from BBO500, all samples show the nanosheets structures, indicating that the cathodic potentials could not only modify the electronic properties of Bi centers, but also lead to rapid self-reconstruction in nanostructures. HRTEM in conjunction with EDX mapping and the corresponded line scans were employed to characterize three representative samples, namely, BBO100, BBO1000 and BBO3000, to uncover the evolution process of BBO (Fig. 2). In the initial stage of reduction (BBO100), nanosized Bi were clearly exsolved on the surface of BBO, leading to the intermediate Bi/BBO structures where the unreacted BBO core is covered by the Bi shell. This observation is in accordance with XRD and FESEM results. As the reduction prolongs to

1000s, the BBO phase is hardly maintained, as revealed by the much weaker intensity of Ba signal compared to BBO100. Noteworthy, the majority of BBO should have converted to Bi at this point due to the severe BBO dissolution. As the reaction time extends to 3000s, only the Bi nanosheets can be identified by both the FESEM and TEM, and the thickness of randomly selected BBO3000 was determined as 0.8 and 1.3 nm, roughly two to four atomic layers, which is the typical range for Bi metallene (Fig. S7a) [34,35]. The lattice fringes of BBO3000 with d-spacing of 0.39 nm corresponds to the (003) facets of metallic bismuth (Fig. S7b), confirming the conversion from pristine BBO to metallic Bi [34]. The Ba background signal in EDX observed in BBO3000 may be attributed to the minor unreacted BBO remnant or the possible  $\text{Ba}^{2+}$  adsorption on the material surface. The TEM images of other randomly selected regions of BBO3000 are shown in Fig. S8. The dissolution of BBO scaffolds is further evidenced by the comparing the  $C_{dl}$  values obtained over BBO samples with various reduction times (Fig. S9). Interestingly, the  $C_{dl}$  value gradually decreases as the reduction reaction proceeds over BBO, i.e., the  $C_{dl}$  was calculated as 5.93 and 2.30 mF  $\text{cm}^{-2}$  over BBO100 and BB05000, respectively, and this can be attributed to the gradual loss of Ba sites. Furthermore, the ECSA value of all BBO-based samples was determined, as shown in Fig. S10. Despite the gradual loss of Ba sites, all BBO samples possess larger ECSA compared to that of the commercial Bi nanoparticles. Such morphology of 2D nanosheets is desirable for  $\text{CO}_2\text{RR}$  due to the maximized specific surface area, which guarantees larger contact areas between the catalysts surface and electrolyte. Moreover, the lamellar structures also endow the reduced catalyst thickness on electrode and lower the mass transfer resistance at the solid/liquid interface during  $\text{CO}_2\text{RR}$ , which in turn leads to a higher current density/reaction rate. In addition, the atomic sites at the edges of the 2D nanosheets possess multiple unsaturated chemical bonds and the dangling bonds, therefore, are more active in comparison to the atoms residing in the metal core [22,32], thus achieving the higher catalytic activities. The edge atoms of the ultrathin nanosheets could also help reduce the activation barrier and stabilize certain reaction intermediates, making the reaction more feasible [34].

The validity of the gradual  $\text{Ba}^{2+}$  loss is supported by quantifying the

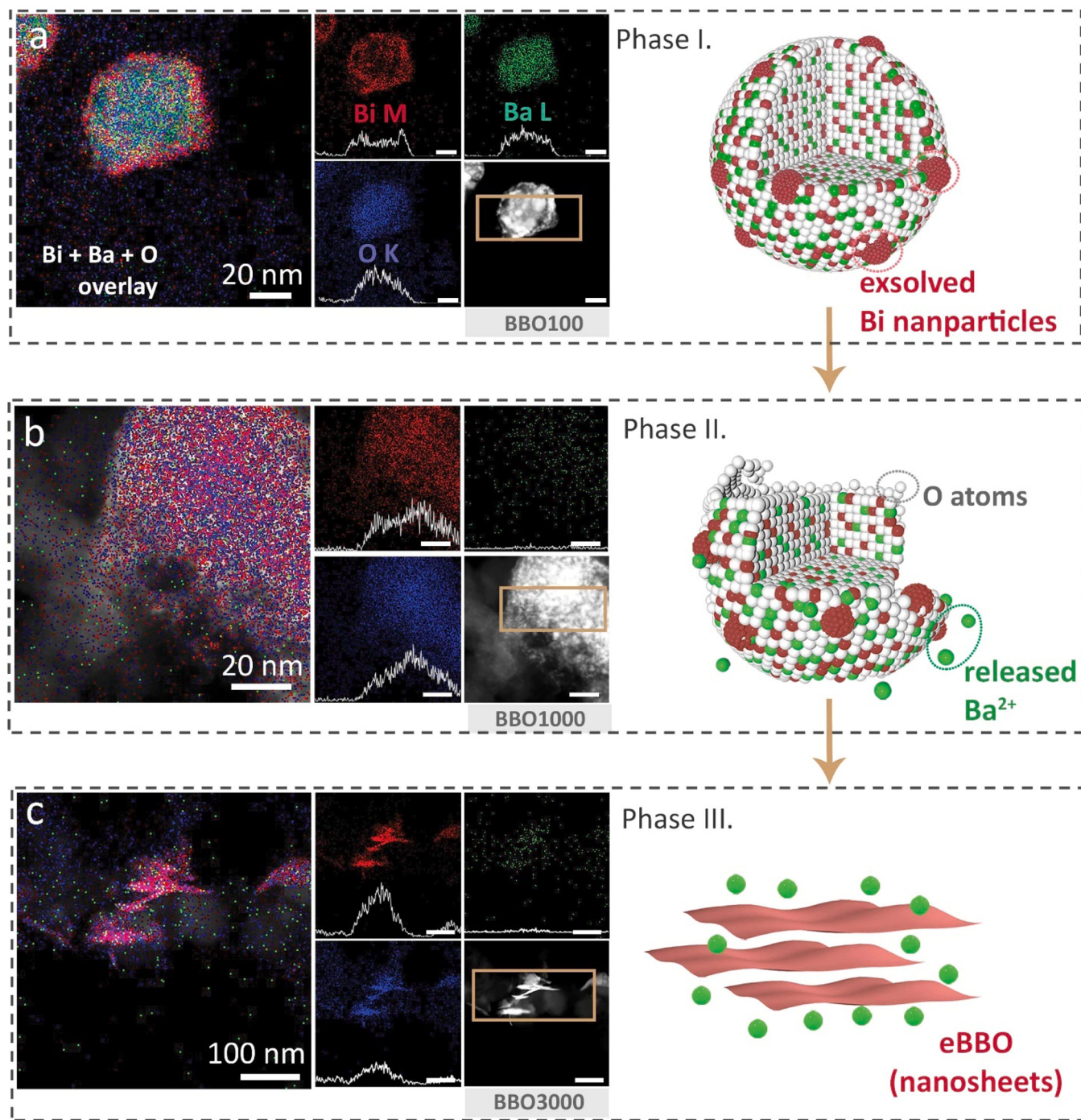


**Fig. 2.** HAADF-STEM dark field images, the EDX mappings and the corresponding schematic illustration of the structures of (a) BBO100, (b) BBO1000 and (c) BBO3000 (cartoon: red: Bi; green: Ba; white: oxygen) to uncover the BBO reduction.

$\text{Ba}^{2+}$  concentration in the used  $\text{KHCO}_3$  (referred to the electrolyte used for BBO3000 preparation) by inductively coupled plasma optical emission spectrometry (ICP-OES). The average  $\text{Ba}^{2+}$  concentration is determined to be  $3.69 \text{ mg L}^{-1}$  after reducing  $1.0 \text{ mg}$  BBO for  $3000 \text{ s}$ . We repeated the electrolysis in  $\text{CO}_2$ -saturated DIW without  $\text{KHCO}_3$  additive, and only identified a much lower  $\text{Ba}^{2+}$  concentration ( $0.097 \text{ mg L}^{-1}$ ). Therefore, both the external bias and the high conductivity of electrolyte appear to facilitate the  $\text{Ba}^{2+}$  release from BBO backbones. Furthermore, to rule out the self-dissolution of BBO in DIW, a fresh piece of BBO was placed in DIW for  $3000\text{s}$  without applied voltage and as expected, no  $\text{Ba}^{2+}$  release was detected, suggesting the structural stability of BBO under potential-free conditions in DIW. The analyses of XRD, Raman,

XPS, and ICP-OES collectively confirmed the BBO-to-Bi conversion upon extended electrochemical conditioning, accompanied by the  $\text{Ba}^{2+}$  release from the perovskite scaffolds due to the overall structural rearrangement.

It is interesting to note that  $\text{La}_2\text{CuO}_4$  (LCO), a perovskite candidate for  $\text{CO}_2\text{RR}$ , partly transforms to  $\text{La}_2\text{O}_3/\text{Cu}$  rather than  $\text{La}^{2+}$  ions (dissolves in the electrolyte) and Cu under similar cathodic potentials [12]. The discrepancy in the final status of A-site elements in LCO and BBO may be ascribed to the pristine perovskite structures and solubility of A-oxides. LCO is a  $\text{K}_2\text{NiF}_4$  type perovskite, where  $\text{Cu}_2\text{O}$  layer and a rock salt  $\text{LaO}$  layer is alternatively stacked (Fig. S11b). Therefore, the exsolution of Cu triggers the break of Cu-O bonds while partly preserving the

integrity of in-plane La-O bonds. Moreover,  $\text{La}_2\text{O}_3$  is insoluble in water. Contrarily, BBO is a  $\text{ABO}_3$  structure, and  $\text{BaO}$  is soluble, and therefore the cleavage of Bi-O and Ba-O bonds will bring about near-complete Ba loss. The final status of A-site element is completely different in LCO and BBO, and therefore A-site could affect the performances of catalysts via distinct mechanisms in the two cases. To be more specific, the  $\text{La}_2\text{O}_3$  formed from LCO may potentially alter the proton activity since  $\text{La}_2\text{O}_3$  is almost inert to  $\text{CO}_2\text{RR}$  but may regulate the  $^*\text{H}$  adsorption and modify selectivity of  $\text{CO}_2\text{RR}$  over HER. In our study,  $\text{Ba}^{2+}$  ions exist in ionic form and remain in the electrolyte. To point out, whilst the perturbation of  $\text{Ba}^{2+}$  could be circumvented by replacing the reacted electrolyte with fresh ones, the  $\text{Ba}^{2+}$  could still interact with  $\text{CO}_2$  conversion since it has been widely accepted that alkaline metal ions could significantly affect  $\text{CO}_2\text{RR}$ , which will be discussed in the following content.

To briefly sum up, conventional exsolution process generally produces nanoparticles grown homogeneously on the surface of host perovskites, and the mild exsolution of B-site elements produces suitable amount of vacancies while maintaining structural integrity [24]. However, from the above results and discussions, it is concluded that electrochemical conditioning can trigger Bi exsolution from BBO backbones in an instantaneous manner. Furthermore, Bi exsolution only ceases upon complete reorganization of BBO, which results in the complete phase transformation from BBO to Bi. The catalyst reconstruction route is, in essence, a Bi dissolution-renucleation-growth pathway. At the moderate potential of - 1.2 V, Bi in BBO is continuously reduced, and any remaining exsolvable Bi ions would keep diffusing from interior towards electrode/electrolyte interface until reaching an equilibrium, leading to the nucleation of Bi at electrode surface followed by the in situ preferential growth of Bi nanosheets. Meanwhile, the released  $\text{Ba}^{2+}$  ions are dissolved into the aqueous electrolyte and remain in the ionic form.

### 3.3. $\text{CO}_2$ -to-FA conversion on eBBO

To understand whether the phase change of BBO affects the  $\text{CO}_2\text{RR}$  from a thermodynamic point of view, DFT-based calculations were performed to examine the Gibbs free energy changes of  $\text{CO}_2$ -to-FA conversion and HER on pristine BBO and the reconstructed BBO surface (eBBO) (Fig. S12). BBO (100) and BBO (001) slabs were employed to represent the pristine BBO surface because Bi atoms, which are the active centers, can be well exposed on these two surfaces. Bi (003) slab was adopted to represent eBBO surface based on the previous HR-TEM results. The computational results show that the rate determining step (RDS) for  $\text{CO}_2$ -to-FA conversion on Bi (003) is the first protonation step to produce  $^*\text{OCHO}$ , which requires an energy of 1.050 eV, and the subsequent formation of FA is a barrierless step. For BBO (100), the  $^*\text{OCHO}$  intermediate will adsorb to Bi atoms in all considered configurations. The RDS is also the first protonation step to form  $^*\text{OCHO}$  but with a higher energy barrier of 1.21 eV compared to that of the eBBO, indicating that the activation of  $^*\text{CO}_2$  molecule to form  $^*\text{OCHO}$  is more difficult on BBO (100). For BBO (001), we observed an interesting phenomenon: the  $^*\text{OCHO}$  intermediate tends to coordinate with subsurface Ba atoms rather than Bi atoms regardless of the initial adsorption site, and this is perhaps owing to the strong alkalinity of Ba atoms. However, it should be noted that Ba atoms are not the true active centers despite the easiest formation of  $^*\text{OCHO}$  among all surfaces. We also simulated the free energy change of HER on these three different surfaces. For eBBO and BBO (100), the adsorption energies of  $^*\text{OCHO}$  and  $^*\text{H}$  show similar trend due to the existence of the scaling relation. Based on these results, we conclude that the reconstruction of BBO to produce eBBO is desirable, and the eBBO surface favors the FA production by providing suitable  $^*\text{OCHO}$  adsorption energy and the barrierless desorption of FA.

To comprehensively evaluate the  $\text{CO}_2\text{RR}$  activity of the eBBO and to compare eBBO with the reported Bi-based catalysts, we firstly evaluated the electrocatalytic activities of eBBO in 0.1 M  $\text{KHCO}_3$  electrolytes using the H-cell separated by a Nafion 117 membrane (Fig. S13). As shown

from the LSV curves in Fig. 3a, the  $j_{total}$  of eBBO obtained in  $\text{CO}_2$ -bubbled electrolytes is comparatively higher than those in the Argon bubbled media, indicating the occurrence of  $\text{CO}_2$  conversion. The external potential was stepped down from - 0.7 to - 1.3 V to detect the product distributions of potentiostatic  $\text{CO}_2\text{RR}$  electrolysis, and the gaseous and liquidus products over  $\text{CO}_2\text{RR}$  were examined by adopting online GC and offline IC in sequence (Fig. 3b). The results unveil that the liquid phase is composed of FA over the entire measured voltage range, whereas  $\text{H}_2$  and CO account for the rest gaseous phases. The  $\text{FE}_{\text{HCOO}^-}$  exceeds 90.0% as the potential shifts more negatively to - 0.9 V, and the maximum  $\text{FE}_{\text{HCOO}^-}$  approaching 100% has been achieved at - 1.2 V, accompanied with 0.3% of  $\text{H}_2$  and 1.0% of CO. The  $\text{FE}_{\text{HCOO}^-}$  slightly deteriorates to 93.1% by further raising the potential to - 1.3 V, and the enhanced hydrogen evolution reaction (HER) at - 1.3 V may be ascribed to the limited  $\text{CO}_2$  mass transfer. Furthermore, the FA partial current densities ( $j_{\text{HCOO}^-}$ ) obtained from the steady-state current densities and  $\text{FE}_{\text{HCOO}^-}$  confirm the excellent  $\text{CO}_2$ -to-FA conversion on eBBO catalyst (Fig. 3b, and S14). Especially, the high  $j_{\text{HCOO}^-}$  of - 20.7 mA cm<sup>-2</sup> can be obtained at a moderate potential of - 1.2 V, along with a FA production rate of 533.2  $\mu\text{mol h}^{-1} \text{cm}^{-2}$  (Fig. S15). The FEs obtained over eBBO from 0.5 M  $\text{KHCO}_3$  exhibit the similar trend, peaking at - 1.0 V with a  $\text{FE}_{\text{HCOO}^-}$  of 92.3% (Fig. S16). A control experiment using only argon as the feed gas produces almost exclusively  $\text{H}_2$  and a trace amount of CO and FA (Fig. S17). The minor amounts of CO and FA come from the electrolysis of  $\text{HCO}_3^{-1}$ , which is a common phenomenon in  $\text{KHCO}_3$  based electrolyte owing to the dynamic equilibrium between dissolved  $\text{CO}_2$  and  $\text{HCO}_3^{-1}$  [36]. Furthermore, no FA has been acquired over bare carbon paper substrate (Fig. S18), affirming the catalytic roles of eBBO rather than carbon substrate. Fig. S18 It is well known that the evolution of  $\text{H}_2$  from water splitting ( $2\text{H}_2\text{O} \rightarrow \text{O}_2 + 2\text{H}_2$ ) always outcompetes the  $\text{CO}_2\text{RR}$  and consequently, hampers the efficiency and selectivity of  $\text{CO}_2\text{RR}$  in aqueous media. For example, the maximum  $\text{FE}_{\text{HCOO}^-}$  has been identified as 85.7% at - 1.2 V for commercial Bi nanoparticles with larger particle sizes (Fig. S19). Clearly, the Bi ultrathin nanosheets benefit the  $\text{CO}_2\text{RR}$  by effectively suppressing the HER. Overall, the eBBO developed in this study exhibits a well-suppressed HER with  $\text{FE}_{\text{H}_2}$  maintaining at lower than 3.0% from - 1.0 to - 1.3, and  $\text{FE}_{\text{HCOO}^-} > 90\%$  over a wide potential range of at least 400 mV in 0.1 M  $\text{KHCO}_3$  solution, suggesting that the eBBO derived from perovskite is a good catalyst capable of selectively acquiring FA with high activity.

The electrochemical stability of catalysts is another important criterion to evaluate a catalyst for  $\text{CO}_2\text{RR}$  in addition to the catalytic selectivity. Thus, we examined the long-term durability of eBBO at the negative bias of - 1.2 V, and the electrolyte was replaced with fresh ones periodically (around every 6.5 h) during the test (Fig. 3c). The eBBO achieves the stable operation over 60 h at an average current density of - 21.0 mA cm<sup>-2</sup> with a  $\text{FE}_{\text{HCOO}^-}$  retention of 90.0% (which corresponds to a  $\text{FE}_{\text{HCOO}^-} = 90.1\%$  at the end of the 60 h test). The above analysis indicates that eBBO possesses a great potential as a promising candidate for  $\text{CO}_2\text{RR}$  with the superior FA selectivity ( $\text{FE}_{\text{HCOO}^-} \approx 99\%$  at - 1.2 V) and durability (60 h at - 1.2 V with a  $\text{FE}_{\text{HCOO}^-}$  retention of 90%). The post-mortem characterizations after the long-term stability tests of 12 h and 60 h (denoted as eBBO-12 and eBBO-60) were performed to study the eBBO at the different stages of  $\text{CO}_2\text{RR}$ . As shown in Figs. S20a and S20b, the XRD and Raman spectra confirm the dominance of  $\text{Bi}^0$  phase after long-time electrolysis of  $\text{CO}_2$ . The SEM image of eBBO-12 reveals the well-preserved lamellar structure of eBBO (Fig. S20c), which gradually evolved to porous Bi sheets composed of ultrasmall nanoparticles upon the extended reaction time of 60 h (Fig. S20d), as further confirmed by the exposed (110) facet of Bi and EDX mappings (Fig. S20e and S20f). Despite the emergence of the ultrasmall Bi nanoparticles, the nanosheets structures are still partly preserved. Therefore, the eBBO obtained in this study shows a good stability during the long-term tests at a very negative potential of -1.2 V For comparison, the important merits of the recently reported Bi-based catalysts have been summarized

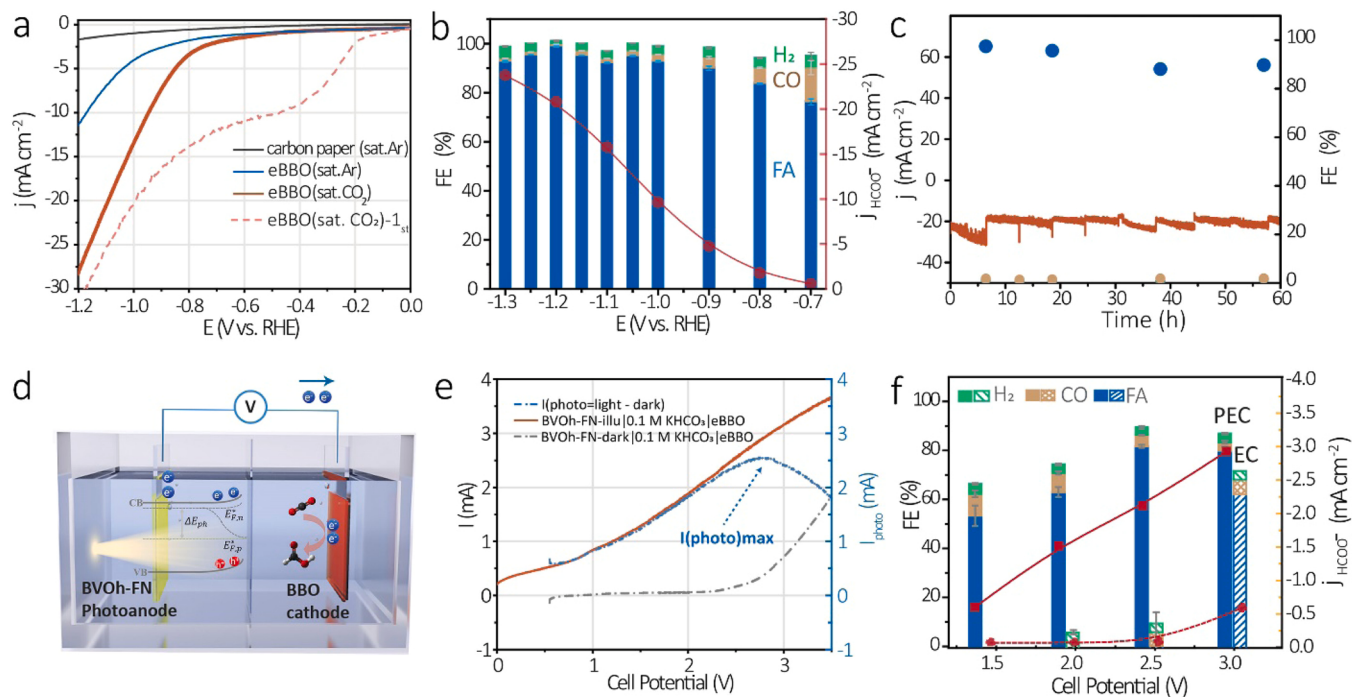


**Fig. 3.** (a) LSV curves of eBBO at a scan rate of  $0.05 \text{ V s}^{-1}$ . (b) Potential-dependent FEs of  $\text{H}_2$ ,  $\text{CO}$ , and FA on eBBO. (c) Long-term stability tests of eBBO at  $-1.2 \text{ V}$  in  $0.1 \text{ M KHCO}_3$  electrolyte. (d) Schematic illustration of the PEC device. (e) LSV curves for  $\text{BVOh-FN-illu}|0.1 \text{ M KHCO}_3|\text{eBBO}$ ,  $\text{BVOh-FN-dark}|0.1 \text{ M KHCO}_3|\text{eBBO}$ , and corresponded  $I_{\text{photo}}$  (photocurrent) as a function of cell potential in two-electrode cells. (f) Potential-dependent FEs and partial current densities for FA in  $\text{BVOh-FN}|0.1 \text{ M KHCO}_3|\text{eBBO}$  PEC and EC cells.

in Table S3. The eBBO developed in this study is among one of the best Bi-based catalysts reported so far. More practically, the facile synthesis procedure and the low cost of  $\text{BaBiO}_3$  render it suitable for industrial-scale implementations.

As stated before, zero net emission of  $\text{CO}_2$  can be realized by utilizing renewable energy to drive  $\text{CO}_2$ RR. Inspired by the excellent  $\text{CO}_2$ - to - FA conversion on eBBO surface, we explored the opportunity to drive the reaction partially using clean and renewable solar energy by wiring the eBBO dark cathode with a low-cost  $\text{BiVO}_4$  photoanode (deposited with  $\text{FeOOH}$  and  $\text{NiOOH}$  layers) for the OER reaction to construct a PEC ( $\text{BVOh-FN}|0.1 \text{ M KHCO}_3|\text{eBBO}$ , Fig. 3d). The XRD, SEM, and UV-vis characterizations of BVO photoanodes are shown in Fig. S21a-c, which confirm the successful preparation of BVO anode. Illuminated LSV analysis was carried out to determine the photocurrent densities of BVOh-FN as a function of the applied potentials (Fig. S21d), which provides useful information on the optimal operation voltages in the PEC cell. The theoretical operational voltage of the two-electrode cell at a certain current density can be determined by the differences between the corresponding potentials of photoanode and cathode (Fig. S22). Thus, to unveil the optimal working conditions of  $\text{BVOh-FN}|0.1 \text{ M KHCO}_3|\text{eBBO}$ , the illuminated/dark LSV signals of eBBO coupled with BVOh-FN were firstly collected at the cell potentials from 0 to 3.5 V (Fig. 3e). It is observed that the dark current of  $\text{BVOh-FN}|0.1 \text{ M KHCO}_3|\text{eBBO}$  remains comparably small when the cell potentials stay below 2.0 V. As the potentials shift upward, the dark currents start to contribute a non-negligible portion to the total current ( $I$ ). For instance, the current flowing through the PEC cell reaches 1.2 mA at 3 V. Fig. S23 is the recorded periodic current responses obtained in EC and PEC cells, in agreement with the LSV results. The photo current,  $I_{\text{photo}}$ , determined by finding the difference between the currents measured under dark and light conditions in  $\text{BVOh-FN}|0.1 \text{ M KHCO}_3|\text{eBBO}$  is shown in Fig. 3e (blue line). A closer examination at  $I_{\text{photo}}$  reveals that  $I_{\text{photo}}$  reaches the maximal value at a cell voltage of around 2.75 V, which is the vertex of the parabola. To better distinguish between the contributions of solar and electricity energy inputs, the cathode potential and the

corresponding  $I$  are monitored as a function of the applied potentials on photoanode, and the results are shown in Fig. S24. Apparently, the potential of dark cathode increases rapidly when the anodic potential increases from 0.5 to 1.1 V, but the rate gradually decreases as the anode potential exceeds 1.1 V (Point K). Furthermore, the current increase rate in the anodic potential range of 0.5 – 1.1 V is clearly much higher than that in the 1.1 – 2 V range, suggesting a more efficient utilization of solar energy in the potential range of 0.5 – 1.1 V. These results collectively point out that the maximal utilization of solar energy can be accomplished approximately at the point K where the cell voltage of around 2 V with a total current of 2.5 mA is achieved. This result is slightly at variance with the data obtained from LSV results, which is presumably ascribed to the rapid scan rate of LSV. In light of all the experimental evidence, the overall operational voltages should be in the range of 2.0 – 2.75 V in the  $\text{BVOh-FN}|0.1 \text{ M KHCO}_3|\text{eBBO}$  for PEC device to truly benefit from solar energy.

The selectivity of products in PEC and EC under the optimized working conditions is shown in Fig. 3f. It is found that FA can be generated with the  $\text{FE}_{\text{HCOO}^-}$  of 59.0% and 63.3% at the cell voltages of 1.5 and 2 V in PEC device, respectively, and the  $\text{FE}_{\text{HCOO}^-}$  gradually raises to 80.0% at a cell voltage of 2.5 V with  $j_{\text{HCOO}^-}$  of  $-2.1 \text{ mA cm}^{-2}$ . Further increasing cell potential to 3 V yields a higher  $\text{FE}_{\text{HCOO}^-}$  of 81.0%, and the  $j_{\text{HCOO}^-}$  reaches  $-2.9 \text{ mA cm}^{-2}$  (Fig. S25). Contrarily, no FA is detected in EC at 1.5 nor at 2 V, and  $\text{FE}_{\text{HCOO}^-} < 1.0\%$  is detected at 2.5 V with a negligible  $j_{\text{HCOO}^-}$  of  $-0.015 \text{ mA cm}^{-2}$ . It is only when the external bias reaches 3.0 V that the EC cell will start to contribute significantly to FA production (i.e.,  $\text{FE}_{\text{HCOO}^-} = 60.1\%$ ). Based on the above results, it can be concluded that solar energy can compensate for a portion of the external bias needed to drive the  $\text{CO}_2$ RR and can favorably shift the onset potential for FA generation to a smaller value, thereby achieving an appreciable current and FEs for target products compared to the pure electricity-driven approach. Consequently, the PEC cell realizes a high FA selectivity of 80% at the cell voltage of 2.5 V where trivial amount of FA is detected at the same potential in EC cell without solar irradiation.

### 3.4. Effects of Ba cations on CO<sub>2</sub>RR

The electrochemical performance of the eBBO electrode (in Section 3.3) was examined in fresh electrolytes to preclude any possible perturbations of any surface or and naturally released Ba<sup>2+</sup> in the electrolyte. For practical applications, the effects of Ba<sup>2+</sup> should not be ignored since previous studies showed that the alkaline metal ions play a significant role in dictating the FE [37–39]. While many studies have focused on the monovalent cations (i.e., Li<sup>+</sup>, Na<sup>+</sup>, K<sup>+</sup>, etc.), recent studies by Koper et al. showed that the multivalent with larger hydration radii might have even stronger impact over the performances of CO<sub>2</sub>RR since they are more likely to stabilize CO<sub>2</sub>, which is the key to initiate CO<sub>2</sub>RR [40]. The hydrated radii of K<sup>+</sup> and Ba<sup>2+</sup> are 3.31 and 4.04 Å at 25 °C, respectively [41], and theoretically, the Ba<sup>2+</sup>-CO<sub>2</sub> interactions should be more pronounced compared to that of the K<sup>+</sup>-CO<sub>2</sub>. However, in another study by Wallace et al., the CO<sub>2</sub>RR can be greatly suppressed in the seawater-like electrolyte containing 20 mM CaCl<sub>2</sub> due to the formation of calcium carbonate at the electrode surface at applied cathodic potentials [42]. Therefore, the concentration of certain multivalent cations must be well controlled to benefit CO<sub>2</sub>RR.

To gain insights into how the released Ba<sup>2+</sup> from BBO affects CO<sub>2</sub>RR, a series of potential-controlled electrolysis from -0.7 to -1.3 V were conducted to examine the product distributions in 0.1 M KHCO<sub>3</sub> containing 0.025 mM BaCl<sub>2</sub> to mimic the naturally released Ba<sup>2+</sup> when reducing 1.0 mg BBO. As shown in Fig. 4a, the FEs of FA, H<sub>2</sub> and CO obtained in the two electrolytes are almost overlapped, suggesting that the low Ba<sup>2+</sup> concentration (i.e., 0.025 mM) has negligible effects on the CO<sub>2</sub> reduction in 0.1 M KHCO<sub>3</sub> media and therefore BaBiO<sub>3</sub> is suitable for CO<sub>2</sub>RR when KHCO<sub>3</sub> was chosen as electrolyte. However, in 0.1 M KCl-based electrolytes with/without 0.025 mM Ba<sup>2+</sup> additive, a stark difference in FEs can be observed (Fig. 4b) although  $j_{total}$  obtained on eBBO in CO<sub>2</sub>-saturated Ba<sup>2+</sup>-free 0.1 M KCl (pH = 4.0) are very similar to those in the Ba<sup>2+</sup>-containing KCl solution (Fig. S26). In general, the FE<sub>H<sub>2</sub></sub> values in Ba<sup>2+</sup>-containing 0.1 M KCl solutions are always lower than that of the Ba<sup>2+</sup>-free ones in the potential range of -0.9 to -1.2 V, and meanwhile, the FE<sub>HCOO<sup>-</sup></sub> is clearly boosted by Ba<sup>2+</sup> in the electrolyte, especially at less negative potentials (i.e., -0.8 to -1.1 V). This observation is in accordance with previous studies [43]. The changes in the selectivity for FA at these potentials are closely related to the

attenuated HER as the FE<sub>CO</sub> remains relatively constant over the studied potential range (fluctuating within a relatively small range of ± 1.5%), which is presumably owing to the capability of Ba<sup>2+</sup> ions to repel H<sup>+</sup> near the electrode surface. Increasing the Ba<sup>2+</sup> concentration to 2.5 mM (which is 100 times higher than the actual concentration detected in this study) has led to an even more prominent growth in FA production (Fig. S27), suggesting that Ba<sup>2+</sup> additive has indeed contributed to the CO<sub>2</sub>RR reaction in 0.1 M KCl. Notably, further increasing Ba<sup>2+</sup> concentration to 25.0 mM results in the formation of BaCO<sub>3</sub> precipitates when the electrolysis was performed at -1.3 V for 3000 s (Fig. S28a and b), which can be detrimental to CO<sub>2</sub>RR since BaCO<sub>3</sub> could block the Bi active sites, retard efficient mass and electron transfers and thus, impede efficient CO<sub>2</sub>RR electrolysis. It should be noted that in real cases, however, such a high Ba<sup>2+</sup> concentration in the electrolyte is unlikely to occur.

To understand how Ba<sup>2+</sup> interplays with the CO<sub>2</sub> molecules, the time-resolved FTIR studies were carried out. Certain amount of BaCl<sub>2</sub> was dipped on the clean eBBO electrode and then dried overnight prior to usage (named Ba<sup>2+</sup>-eBBO, assuming all the released Ba<sup>2+</sup> has been adsorbed to the surface). As shown in Fig. 4c and d, both eBBO and Ba<sup>2+</sup>-eBBO samples show prominent peaks at 2200–2400 cm<sup>-1</sup>, which can be attributed to the physical adsorption of CO<sub>2</sub>. The CO<sub>2</sub> adsorption responses of both samples could stabilize at around 60 mins, however, the signal intensities in Ba<sup>2+</sup>-eBBO sample are apparently higher than that of the bare eBBO surface. For example, the peak heights in Ba<sup>2+</sup>-eBBO were already larger than the bare eBBO when the reaction only proceeded for 10 mins. Therefore, the intensified FTIR signals in Ba<sup>2+</sup>-eBBO indicate that Ba<sup>2+</sup> favors the CO<sub>2</sub> adsorption, in line with previous studies [44]. To identify possible reaction intermediates of CO<sub>2</sub>RR in 0.1 M KCl and 0.025 mM Ba<sup>2+</sup> added 0.1 M KCl (Ba<sup>2+</sup>-KCl), in situ Raman analysis was then performed over eBBO to gain mechanistic insights. As shown in Fig. 4e, both the samples exhibit two characteristic Raman shifts at 1313 and 1616 cm<sup>-1</sup> which are assigned to the glassy carbon substrate. In Ba<sup>2+</sup>-KCl media, a marked Raman peak at around 1061 cm<sup>-1</sup> can be clearly observed in a wide potential range, i.e., at -0.8 V and more negative potentials. This peak is ascribed to the symmetric stretching oscillation of carbonate ( $\nu_1 CO_3^{2-}$ ) [45,46]; whereas no  $\nu_1 CO_3^{2-}$  bands can be identified on the eBBO surface measured in pure KCl electrolyte. The formation of BaCO<sub>3</sub> can be ruled out, since the

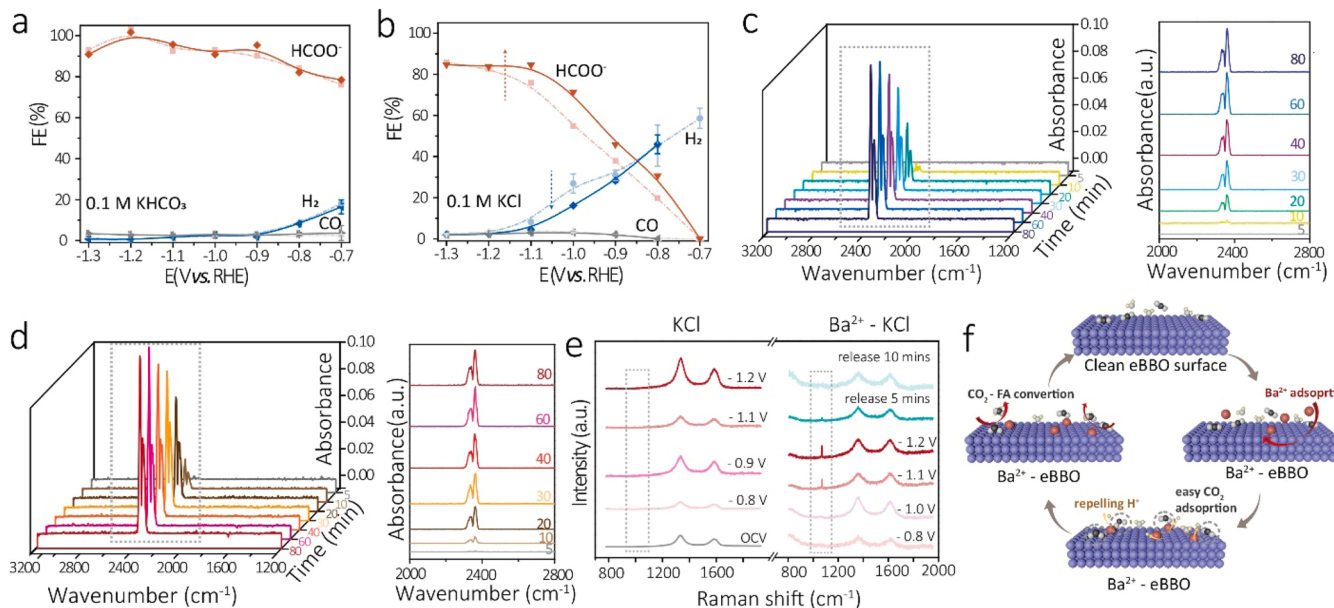


**Fig. 4.** Potential dependent FEs over eBBO in (a) 0.1 M KHCO<sub>3</sub> and (b) 0.1 M KCl electrolyte with (solid lines) or without 0.025 mM BaCl<sub>2</sub> (dash lines) addition. Time-resolved FTIR studies of (c) eBBO and (d) Ba<sup>2+</sup>-eBBO. (e) *In situ* Raman analysis of eBBO in 0.1 M KCl and Ba<sup>2+</sup>-0.1 M KCl performed under various external potentials. (f) Proposed working mechanism of the eBBO with natural released Ba<sup>2+</sup> in the electrolyte for the selective FA production from CO<sub>2</sub>RR.

$\nu_1CO_3^{2-}$  band gradually decreases and eventually vanishes upon releasing the applied potential (-1.2 V). This observation indicates that the Ba<sup>2+</sup> in the 0.1 M KCl electrolyte has led to enhanced adsorption of carbonate intermediate, which evidently promotes the CO<sub>2</sub>-to-FA conversion. Song et al. reported similar results over S-doped Cu for highly selective production of FA, and their study shows that S-doped Cu exhibit much enhanced  $\nu_1CO_3^{2-}$  adsorption compared to that of the undoped Cu samples [41].

In fact, previous studies have also carefully examined cation effects by analyzing their perturbations on internal electric field [47–49]. Although most of the reported studies are based on the monovalent cations/anions (i.e., Li<sup>+</sup>, K<sup>+</sup>, Cs<sup>+</sup>, Na<sup>+</sup>, Cl<sup>-</sup>, I<sup>-</sup>, Br<sup>-</sup>), one can still expect the roles of multivalent ions in the electrical field to be even more significant. The “electrolyte-defined selectivity” for CO<sub>2</sub>RR is perhaps related to the different local CO<sub>2</sub> environment and CO<sub>2</sub>-cation interactions near the catalyst surface in the two electrolytes. It is well acknowledged that KHCO<sub>3</sub> solutions can create a high local CO<sub>2</sub> concentration due to the equilibrium between bicarbonate and dissolved CO<sub>2</sub>, meaning that the CO<sub>2</sub> consumed at surface can be rapidly replenished by bicarbonate [50]. As a result, the Ba<sup>2+</sup> mediated CO<sub>2</sub> adsorption could only contribute a negligible amount to the total CO<sub>2</sub> concentration on electrode surface, and therefore the FEs of all products remain very similar in the electrolytes with/without Ba<sup>2+</sup> addition. However, in 0.1 M KCl, the CO<sub>2</sub> is replenished by the dissolved CO<sub>2</sub>, which is insufficient in amount compared to that in the KHCO<sub>3</sub>-based solutions considering the low CO<sub>2</sub> solubility in the water-based electrolyte. In such a case, even the trace amount of Ba<sup>2+</sup> (i.e., 0.025–2.5 mM) in 0.1 M KCl may lead to an effective enhancement in the local CO<sub>2</sub> concentration and therefore remarkably boost CO<sub>2</sub>RR over HER, since Ba<sup>2+</sup> has been shown to favor CO<sub>2</sub> adsorption based on the previous analysis. In a recent study by Bell et al., they also suggested that the local CO<sub>2</sub> concentration can be regulated by the hydrolysis of alkaline metal ions, and the CO<sub>2</sub> concentration improves with increasing the cation size [51]. To confirm our hypothesis, further studies that incorporate multiple *in situ* techniques are required to fully unveil the effects of Ba<sup>2+</sup>. Nonetheless, based on our extensive electrochemical characterizations, it can therefore be concluded that the Ba<sup>2+</sup> released from BBO should be beneficial to FA production in general despite that these effects are collectively dependent on the external potentials, type of electrolytes, as well as the Ba<sup>2+</sup> concentration. It should be emphasized that final concentration of Ba<sup>2+</sup> in the electrolytes is determined by the loading mass of catalyst, as well as the total volume of electrolyte, and these parameters may vary depending on the real operation conditions of CO<sub>2</sub>RR.

Finally, we consider the eBBO with naturally released Ba<sup>2+</sup> as one system, and the working mechanisms for CO<sub>2</sub>-to-FA are proposed, as shown in Fig. 4f. Firstly, the adsorption of Ba<sup>2+</sup> will take place at the eBBO surface at cathodic potentials. Secondly, the CO<sub>2</sub> dissolved in the electrolyte can be adsorbed more easier on Ba<sup>2+</sup> sites and/or Bi sites adjacent to Ba<sup>2+</sup>, leading to higher local CO<sub>2</sub> concentration compared to that of the bare Bi surface. Afterwards, the adsorbed CO<sub>2</sub> would gain one electron and form CO<sub>2</sub><sup>-</sup> intermediate, following the hydrogenation step to form HCOO<sup>•(ads)</sup> which further proceeds the elementary step of HCOO<sup>•(ads)</sup> + e<sup>-</sup> → HCOO<sup>-(ads)</sup>, as proposed in the CO<sub>2</sub>-to-FA mechanisms on Bi surface by a previous study [52]. In the final step, the HCOO<sup>-(ads)</sup> desorbs from the surface and form the final product HCOO<sup>-(aq)</sup>. Over the entire process, both the Bi catalytic active sites and Ba<sup>2+</sup> ions participate in the CO<sub>2</sub>RR and work cooperatively to drive CO<sub>2</sub>-to-FA conversion, and this mechanism could be extended to other perovskite-based materials for electrocatalytic CO<sub>2</sub>RR at room temperature.

#### 4. Conclusions

In summary, by a series of extensive physical and electrochemical characterizations, we are able to unveil: 1) the structural and phase

evolution of pristine BBO perovskite under cathodic potentials, and that is, the electrochemical conditioning of pristine BBO leads to the *in operando* “dissolution-nucleation-growth” of Bi ions. The resulting eBBO with atomic-scale thickness provides an enlarged active area and more unsaturated active centers, which is among one of the best Bi-based catalysts for FA production reported so far. 2) The cooperative working mechanisms of A- and B- site species in voltage-reconstructed BBO perovskite that regulate the surface reactions. In contrast to the commonly accepted concept that only B-site elements are actively involved in CO<sub>2</sub>RR, our experimental results and systematic analyses demonstrate that the multivalent A-site elements can concurrently participate in CO<sub>2</sub>RR and benefit FA production and furthermore, the Ba<sup>2+</sup> concentration, external potentials and the type of electrolyte play the critical roles in enhancing the beneficial effect of Ba<sup>2+</sup> on CO<sub>2</sub>RR. Our studies show that perovskite-based materials that integrate both A- and B- site elements in one structure, should serve as an effective platform for efficient CO<sub>2</sub>RR with mutual benefits coming from both elements.

#### CRediT authorship contribution statement

**Jing-Li Luo:** Project administration, Supervision, Funding acquisition, Writing – review & editing. **Meng-Nan Zhu:** Conceptualization, Data curation, Methodology, Validation, Computation, Writing – original draft. **Bo-Wen Zhang:** Conceptualization, Data curation. **Min-Rui Gao:** Software. **Peng-Fei Sui:** Data curation. **Chenyu Xu:** Data curation. **Lu Gong:** Data curation. **Hongbo Zeng:** Data curation. **Karthik Shankar:** Writing – review & editing. **Steven Bergens:** Writing – review & editing.

#### Declaration of Competing Interest

The authors declare no competing financial interest.

#### Acknowledgements

This work is supported by the Natural Sciences and Engineering Research Council (NSERC) of Canada Discovery Grant [GRPIN-2016-05494]. As a part of the University of Alberta’s Future Energy Systems research initiative, this research was made possible in part thanks to the funding from the Canada First Research Excellence Fund. The computation sources are provided by Compute Canada and Westgrid.

#### Appendix A. Supporting information

Supplementary data associated with this article can be found in the online version at doi:10.1016/j.apcatb.2022.121101.

#### References

- [1] M. Fan, S. Prabhudev, S. Garbarino, J. Qiao, G.A. Botton, D.A. Harrington, A.C. Tavares, D. Guay, Uncovering the nature of electroactive sites in nanoarchitected dendritic Bi for highly efficient CO<sub>2</sub> electroreduction to formate, Appl. Catal. B Environ. 274 (2020), 119031.
- [2] Z. Chen, M.R. Gao, N. Duan, J.J. Zhang, Y.Q. Zhang, T. Fan, J.J. Zhang, Y. Dong, J. Li, Q. Liu, X. Yi, J.L. Luo, Tuning adsorption strength of CO<sub>2</sub> and its intermediates on tin oxide-based electrocatalyst for efficient CO<sub>2</sub> reduction towards carbonaceous products, Appl. Catal. B Environ. 277 (2020), 119252.
- [3] S. Nitopi, E. Bertheussen, S.B. Scott, X. Liu, A.K. Engstfeld, S. Horch, B. Seger, I.E. L. Stephens, K. Chan, C. Hahn, J.K. Nørskov, T.F. Jaramillo, I. Chorkendorff, Progress and perspectives of electrochemical CO<sub>2</sub> reduction on copper in aqueous electrolyte, Chem. Rev. 119 (2019) 7610–7672.
- [4] P. Wang, M. Qiao, Q. Shao, Y. Pi, X. Zhu, Y. Li, X. Huang, Phase and structure engineering of copper tin heterostructures for efficient electrochemical carbon dioxide reduction, Nat. Commun. 9 (2018) 4933.
- [5] Y.Y. Birdja, E. Pérez-Gallent, M.C. Figueiredo, A.J. Göttle, F. Calle-Vallejo, M.T. M. Koper, Advances and challenges in understanding the electrocatalytic conversion of carbon dioxide to fuels, Nat. Energy 4 (2019) 732–745.
- [6] F. Yang, A.O. Elnabawy, R. Schimmenti, P. Song, J. Wang, Z. Peng, S. Yao, R. Deng, S. Song, Y. Lin, M. Mavrikakis, W. Xu, Bismuthene for highly efficient carbon dioxide electroreduction reaction, Nat. Commun. 11 (2020) 1088.

[7] Q. Gong, P. Ding, M. Xu, X. Zhu, M. Wang, J. Deng, Q. Ma, N. Han, Y. Zhu, J. Lu, Z. Feng, Y. Li, W. Zhou, Y. Li, Structural defects on converted bismuth oxide nanotubes enable highly active electrocatalysis of carbon dioxide reduction, *Nat. Commun.* 10 (2019) 2807.

[8] Z. Wu, H. Wu, W. Cai, Z. Wen, B. Jia, L. Wang, W. Jin, T. Ma, Engineering bismuth–tin interface in bimetallic aerogel with a 3D porous structure for highly selective electrocatalytic CO<sub>2</sub> reduction to HCOOH, *Angew. Chem. Int. Ed.* 60 (2021) 12554–12559.

[9] E. Grabowska, Selected perovskite oxides: characterization, preparation and photocatalytic properties—a review, *Appl. Catal. B Environ.* 186 (2016) 97–126.

[10] D.J. Deka, J. Kim, S. Gunduz, M. Aouine, J.M.M. Millet, A.C. Co, U.S. Ozkan, Investigation of hetero-phases grown via in-situ exsolution on a Ni-doped (La,Sr) FeO<sub>3</sub> cathode and the resultant activity enhancement in CO<sub>2</sub> reduction, *Appl. Catal. B Environ.* 286 (2021), 119917.

[11] J. Hwang, R.R. Rao, L. Giordano, Y. Katayama, Y. Yu, Y. Shao-Horn, Perovskites in catalysis and electrocatalysis, *Science* 358 (2017) 751–756.

[12] S. Chen, Y. Su, P. Deng, R. Qi, J. Zhu, J. Chen, Z. Wang, L. Zhou, X. Guo, B.Y. Xia, B. Yu Xia, Highly selective carbon dioxide electroreduction on structure-evolved copper perovskite oxide toward methane production, *ACS Catal.* 23 (2020) 12.

[13] J. Wang, C. Cheng, B. Huang, J. Cao, L. Li, Q. Shao, L. Zhang, X. Huang, Grain-boundary-engineered La<sub>2</sub>CuO<sub>4</sub> perovskite nanobamboos for efficient CO<sub>2</sub> reduction reaction, *Nano Lett.* 21 (2021) 980–987.

[14] Y. Pi, J. Guo, Q. Shao, X. Huang, All-inorganic SrSnO<sub>3</sub> perovskite nanowires for efficient CO<sub>2</sub> electroreduction, *Nano Energy* 62 (2019) 861–868.

[15] S. Liu, R.-T. Gao, M. Sun, Y. Wang, T. Nakajima, X. Liu, W. Zhang, L. Wang, In situ construction of hybrid Co(OH)<sub>2</sub> nanowires for promoting long-term water splitting, *Appl. Catal. B Environ.* 292 (2021), 120063.

[16] J. Vavra, T.H. Shen, D. Stoian, V. Tileli, R. Buonsanti, Real-time monitoring reveals dissolution/redeposition mechanism in copper nanocatalysts during the initial stages of the CO<sub>2</sub> reduction reaction, *Angew. Chem. - Int. Ed.* 60 (2020) 1347–1354.

[17] H. Jiang, Q. He, Y. Zhang, L. Song, Structural self-reconstruction of catalysts in electrocatalysis, *Acc. Chem. Res.* 51 (2018) 2968–2977.

[18] A. Zhang, Y. Liang, H. Li, B. Zhang, Z. Liu, Q. Chang, H. Zhang, C.-F. Zhu, Z. Geng, W. Zhu, J. Zeng, In-situ surface reconstruction of inn nanosheets for efficient CO<sub>2</sub> electroreduction into formate, *Nano Lett.* 20 (2020) 8229–8235.

[19] D. Mignard, R.C. Barik, A.S. Bharadwaj, C.L. Pritchard, M. Ragnoli, F. Cecconi, H. Miller, L.J. Yellowlees, Revisiting strontium-doped lanthanum cuprate perovskite for the electrochemical reduction of CO<sub>2</sub>, *J. CO<sub>2</sub> Util.* 5 (2014) 53–59.

[20] C.J. Chang, S.C. Lin, H.C. Chen, J. Wang, K.J. Zheng, Y. Zhu, H.M. Chen, Dynamic reoxidation/reduction-driven atomic interdiffusion for highly selective CO<sub>2</sub> reduction toward methane, *J. Am. Chem. Soc.* 142 (2020) 12119–12132.

[21] D. Gao, F. Scholten, B.R. Cuenya, Improved CO<sub>2</sub> electroreduction performance on plasma-activated Cu catalysts via electrolyte design: halide effect, *ACS Catal.* 7 (2017) 5112–5120.

[22] C. Cao, D.D. Ma, J.F. Gu, X. Xie, G. Zeng, X. Li, S.G. Han, Q.L. Zhu, X.T. Wu, Q. Xu, Metal–organic layers leading to atomically thin bismuthene for efficient carbon dioxide electroreduction to liquid fuel, *Angew. Chem. Int. Ed.* 132 (2020) 15014–15020.

[23] J. Zhu, W. Zhang, Y. Li, W. Yue, G. Geng, B. Yu, Enhancing CO<sub>2</sub> catalytic activation and direct electroreduction on in-situ exsolved Fe/MnO<sub>x</sub> nanoparticles from (Pr, Ba)<sub>2</sub>Mn<sub>2-y</sub>Fe<sub>y</sub>O<sub>5+δ</sub> layered perovskites for SOEC cathodes, *Appl. Catal. B Environ.* 268 (2020), 118389.

[24] J.H. Myung, D. Neagu, D.N. Miller, J.T.S. Irvine, Switching on electrocatalytic activity in solid oxide cells, *Nature* 537 (2016) 528–531.

[25] T.W. Kim, K.S. Choi, Nanoporous BiVO<sub>4</sub> photoanodes with dual-layer oxygen evolution catalysts for solar water splitting, *Science* 24 (2014) 343–3108.

[26] G. Luca, D. Gregorio, T. Burdyny, A. Loiudice, P. Iyengar, W.A. Smith, R. Buonsanti, Facet-dependent selectivity of Cu catalysts in electrochemical CO<sub>2</sub> reduction at commercially viable current densities, *ACS Catal.* 10 (2020) 4854–4862.

[27] J. Xiao, M.R. Gao, S. Liu, J.L. Luo, Hexagonal Zn Nanoplates Enclosed by Zn (100) and Zn (002) Facets for Highly Selective CO<sub>2</sub> Electroreduction to CO, *ACS Appl. Mater. Interfaces* 12 (2020) 31431–31438.

[28] V. Wang, N. Xu, J.C. Liu, G. Tang, W.T. Geng, VASPKIT: A User-friendly Interface Facilitating High-throughput Computing and Analysis Using VASP Code, (2019).

[29] R.B. Sandberg, J.H. Montoya, K. Chan, J.K. Norskov, CO-CO coupling on Cu facets: Coverage, strain and field effects, *Surf. Sci.* 654 (2016) 56–62.

[30] M. Talha, Y.W.W. Lee, Raman modes and dielectric relaxation properties of epitaxial BaBiO<sub>3</sub> thin films, *Mater. Res. Express* 7 (2020) 16420.

[31] P. Lamagni, M. Miola, J. Catalano, M.S. Hvid, M.A.H. Mamakhel, M. Christensen, M.R. Madsen, H.S. Jeppesen, X.M. Hu, K. Daasbjerg, T. Skrydstrup, N. Lock, Restructuring metal–organic frameworks to nanoscale bismuth electrocatalysts for highly active and selective CO<sub>2</sub> reduction to formate, *Adv. Funct. Mater.* 30 (2020) 1–11.

[32] M. Zhao, Y. Gu, W. Gao, P. Cui, H. Tang, X. Wei, H. Zhu, G. Li, S. Yan, X. Zhang, Z. Zou, Atom vacancies induced electron-rich surface of ultrathin Bi nanosheet for efficient electrochemical CO<sub>2</sub> reduction, *Appl. Catal. B Environ.* 266 (2020), 118625.

[33] K. Fan, Y. Jia, Y. Ji, P. Kuang, B. Zhu, X. Liu, J. Yu, Curved surface boosts electrochemical CO<sub>2</sub> reduction to formate via bismuth nanotubes in a wide potential window, *ACS Catal.* 10 (2020) 358–364.

[34] W. Zhang, Y. Hu, L. Ma, G. Zhu, P. Zhao, X. Xue, R. Chen, S. Yang, J. Ma, J. Liu, Z. Jin, Liquid-phase exfoliated ultrathin Bi nanosheets: uncovering the origins of enhanced electrocatalytic CO<sub>2</sub> reduction on two-dimensional metal nanostructure, *Nano Energy* 53 (2018) 808–816.

[35] W. Ma, J. Bu, Z. Liu, C. Yan, Y. Yao, N. Chang, H. Zhang, T. Wang, J. Zhang, Monoclinic scheelite bismuth vanadate derived bismuthene nanosheets with rapid kinetics for electrochemically reducing carbon dioxide to formate, *Adv. Funct. Mater.* 2006704 (2020) 1–8.

[36] T. Li, E.W. Lees, Z. Zhang, C.P. Berlinguet, Conversion of bicarbonate to formate in an electrochemical flow reactor, *ACS Energy Lett.* 5 (2020) 2624–2630.

[37] M. Kō, J. Vaes, E. Klemm, D. Pant, Solvents and supporting electrolytes in the electrocatalytic reduction of CO<sub>2</sub>, *SCIENCE* 19 (2019) 135–160.

[38] S. Ringe, K. Chan, E.L. Clark, J. Resasco, A. Walton, B. Seger, A.T. Bell, Understanding cation effects in electrochemical CO<sub>2</sub> reduction Understanding cation effects in electrochemical CO<sub>2</sub> reduction, *Energy Environ. Sci.* 12 (2019) 3001–3014.

[39] X. Li, C.M. Cunathunge, N. Agrawal, H. Contalvo-Castro, J. Jin, M.J. Janik, M. M. Waagele, Impact of alkali metal cations and iron impurities on the evolution of hydrogen on Cu electrodes in alkaline electrolytes, *J. Electrochem. Soc.* 167 (2020), 106505.

[40] M.C.O. Monteiro, F. Dattila, B. Hagedoorn, R. García-muelas, N. López, M.T. M. Koper, Absence of CO<sub>2</sub> electroreduction on copper, gold and silver electrodes without metal cations in solution, *Nat. Catal.* 4 (2021) 654–662.

[41] E.R. Nightingale Jr., Phenomenological theory of ion solvation: effective radii of hydrated ions, *J. Phys. Chem.* 63 (1959) 1381–1387.

[42] C.-Y. Lee, G.G. Wallace, CO<sub>2</sub> electrolysis in seawater: calcification effect and a hybrid self-powered concept, *J. Mater. Chem. A* 6 (2018) 23301–23307.

[43] A. Schizodimou, G. Kyriacou, Electrochimica acta acceleration of the reduction of carbon dioxide in the presence of multivalent cations, *Electrochim. Acta* 78 (2012) 171–176.

[44] D.J. Deka, J. Kim, S. Gunduz, D. Jain, Y. Shi, J.T. Miller, A.C. Co, U.S. Ozkan, Coke formation during high-temperature CO<sub>2</sub> electrolysis over AFeO<sub>3</sub> (A = La/Sr) cathode: effect of A-site metal segregation, *Appl. Catal. B Environ.* 283 (2021), 119642.

[45] I.V. Chernyshova, P. Somasundaran, S. Ponurangam, On the origin of the elusive first intermediate of CO<sub>2</sub> electroreduction, *Proc. Natl. Acad. Sci. U SA* 115 (2018) E9261–E9270.

[46] Z. Pan, K. Wang, K.H. Ye, Y. Wang, H.-Y. Su, B. Hu, J. Xiao, T. Yu, Y. Wang, S. Song, Intermediate adsorption states switch to selectively catalyze electrochemical CO<sub>2</sub> reductions, *ACS Catal.* 10 (2020) 3871–3880.

[47] S. Banerjee, Z.-Q. Zhang, A.S. Hall, V.S. Thoi, Surfactant perturbation of cation interactions at the electrode–electrolyte interface in carbon dioxide reduction, *ACS Catal.* 10 (2020) 9907–9914.

[48] S. Wallentine, S. Bandaranayake, S. Biswas, L.R. Baker, Direct observation of carbon dioxide electroreduction on gold: site blocking by the stern layer controls CO<sub>2</sub> adsorption kinetics, *J. Phys. Chem. Lett.* 11 (2020) 8307–8313.

[49] S. Banerjee, X. Han, V.S. Thoi, Modulating the electrode–electrolyte interface with cationic surfactants in carbon dioxide reduction, *ACS Catal.* 9 (2019) 5631–5637.

[50] M. Dunwell, Q. Lu, J.M. Heyes, J. Rosen, J.G. Chen, Y. Yan, F. Jiao, B. Xu, The central role of bicarbonate in the electrochemical reduction of carbon dioxide on gold, *J. Am. Chem. Soc.* 139 (2017) 3774–3783.

[51] M.R. Singh, Y. Kwon, Y. Lum, J.W. Ager, A.T. Bell, Hydrolysis of electrolyte cations enhances the electrochemical reduction of CO<sub>2</sub> over Ag and Cu, *J. Am. Chem. Soc.* 138 (2016) 13006–13012.

[52] F. Li, G.H. Gu, C. Choi, P. Kolla, S. Hong, T.-S. Wu, Y.-L. Soo, J. Masa, S. Mukerjee, Y. Jung, J. Qiu, Z. Sun, Highly stable two-dimensional bismuth metal–organic frameworks for efficient electrochemical reduction of CO<sub>2</sub>, *Appl. Catal. B Environ.* 277 (2020), 119241.